

Solar wind energy flux observations in the inner heliosphere: First results from Parker Solar Probe

Mingzhe Liu¹, Karine Issautier¹, Nicole Meyer-Vernet¹, Michel Moncuquet¹, Milan Maksimovic¹, J. S. Halekas², J. Huang³, L. Griton⁴, S. Bale^{5,6,7,8}, J. W. Bonnell⁵, A. W. Case⁹, K. Goetz¹⁰, P. R. Harvey⁵, J. C. Kasper^{3,9}, R. J. MacDowall¹¹, D. M. Malaspina¹², M. Pulupa⁵, and M. L. Stevens⁹

¹ LESIA, Observatoire de Paris, Université PSL, CNRS, Sorbonne Université, Université de Paris, 5 place Jules Janssen, 92195 Meudon, France
e-mail: mingzhe.liu@obspm.fr

² Department of Physics and Astronomy, University of Iowa, IA 52242, USA

³ Climate and Space Sciences and Engineering, University of Michigan, Ann Arbor, MI 48109, USA

⁴ IRAP, Université Paul Sabatier, 9 Av du Colonel Roche, BP 4346, 31028, Toulouse cedex 4, France

⁵ Space Sciences Laboratory, University of California, Berkeley, CA 94720-7450, USA

⁶ Physics Department, University of California, Berkeley, CA 94720-7300, USA

⁷ The Blackett Laboratory, Imperial College London, London, SW7 2AZ, UK

⁸ School of Physics and Astronomy, Queen Mary University of London, London E1 4NS, UK

⁹ Smithsonian Astrophysical Observatory, Cambridge, MA 02138 USA

¹⁰ School of Physics and Astronomy, University of Minnesota, Minneapolis, MN 55455, USA

¹¹ Solar System Exploration Division, NASA/Goddard Space Flight Center, Greenbelt, MD, 20771

¹² Laboratory for Atmospheric and Space Physics, University of Colorado, Boulder, CO 80303, USA

Received: October 8 2020; Accepted: December 29 2020

ABSTRACT

Aims. We investigate the solar wind energy flux in the inner heliosphere using 12-day observations around each perihelion of Encounter One (E01), Two (E02), Four (E04), and Five (E05) of Parker Solar Probe (PSP), respectively, with a minimum heliocentric distance of 27.8 solar radii (R_{\odot}).

Methods. Energy flux was calculated based on electron parameters (density n_e , core electron temperature T_c , and suprathermal electron temperature T_h) obtained from the simplified analysis of the plasma quasi-thermal noise (QTN) spectrum measured by RFS/FIELDS and the bulk proton parameters (bulk speed V_p and temperature T_p) measured by the Faraday Cup onboard PSP, SPC/SWEAP.

Results. Combining observations from E01, E02, E04, and E05, the averaged energy flux value normalized to 1 R_{\odot} plus the energy necessary to overcome the solar gravitation ($W_{R_{\odot}}$) is about $70 \pm 14 \text{ W m}^{-2}$, which is similar to the average value ($79 \pm 18 \text{ W m}^{-2}$) derived by Le Chat et al from 24-year observations by Helios, Ulysses, and Wind at various distances and heliolatitudes. It is remarkable that the distributions of $W_{R_{\odot}}$ are nearly symmetrical and well fitted by Gaussians, much more so than at 1 AU, which may imply that the small heliocentric distance limits the interactions with transient plasma structures.

Key words. (Sun:) solar wind—Sun: heliosphere—Sun: corona—Sun: fundamental parameters—plasmas—acceleration of particles

1. Introduction

The question of how the solar wind is produced and accelerated is unsolved since its discovery about sixty years ago (Parker 1958; Neugebauer & Snyder 1962) and Parker (2001) showed that "we cannot state at the present time why the Sun is obliged by the basic laws of physics to produce the heliosphere". An important property of the solar wind is its energy flux, which is similar in the whole heliosphere and in the fast and slow wind (e.g., Schwenn & Marsch 1990; Meyer-Vernet 2006; Le Chat et al. 2009, 2012), and much more so than the particle flux itself. As shown by Le Chat et al. (2009), the energy flux is of a similar fraction of the luminosity for Solar-like and cool giant stars, which suggests that stellar winds may share a basic process for their origin and acceleration. Investigations of the solar wind energy flux in the inner heliosphere are of significant importance for astrophysics, but there are still very few of them.

Meyer-Vernet (2006, 2007) showed that the average solar wind energy flux scaled to one solar radius of about 70 W m^{-2} from long-term Helios and Ulysses observations is close to the average total energy flux of solar flares and 10^{-6} times the solar luminosity – a fraction similar to that of a number of other stars. With a much larger solar wind data set from several spacecraft at various distances and latitudes, Le Chat et al. (2012) found an average value of $79 \pm 18 \text{ W m}^{-2}$ between 1976 and 2012, whereas McComas et al. (2014) found an average value of about 60 W m^{-2} with OMNI data at 1 AU between 2011 and 2014. Helios 1 and 2 orbits ranged from 0.3 to 1 AU (Schwenn et al. 1975), whereas Ulysses operated between 1 and 4 AU (Wenzel et al. 1992). The ongoing, pioneering mission of Parker Solar Probe (PSP) (Fox et al. 2016) orbits with perihelia of heliocentric distances decreasing from 35.7 solar radii (R_{\odot}) to 9.86 R_{\odot} within five years. Four instruments onboard PSP, including the Fields experiment (FIELDS) (Bale et al. 2016), Solar Wind

Electrons Alphas and Protons investigation (SWEAP) (Kasper et al. 2016), Integrated Science Investigation of the Sun (IS \odot IS) (McComas et al. 2016), and Wide-field Imager for Solar PRobe (WISPR) (Vourlidis et al. 2016), are working together to provide both in situ and remote observations. In situ field and plasma measurements of the inner heliosphere from FIELDS/PSP and SWEAP/PSP offer an opportunity to estimate the solar wind energy flux closer to the Sun than previously derived.

FIELDS/PSP provides accurate electron density and temperature measurements via quasi-thermal noise (QTN) spectroscopy. This technique has been used in a number of space missions (e.g., Meyer-Vernet 1979; Meyer-Vernet et al. 1986; Meyer-Vernet et al. 2017; Issautier et al. 1999, 2001, 2008; Maksimovic et al. 1995; Moncuquet et al. 2005, 2006), and it is an effective and efficient tool. Recently, Moncuquet et al. (2020) and Maksimovic et al. (2020) derived preliminary solar wind electron measurements from the plasma QTN spectra observed by the Radio Frequency Spectrometer (RFS/FIELDS) (see Pulupa et al. 2017). SWEAP/PSP consists of the Solar Probe Cup (SPC) and the Solar Probe Analyzers (SPAN) (Kasper et al. 2016; Case et al. 2020; Whittlesey et al. 2020). SPC is a fast Faraday cup designed to measure the one dimensional velocity distribution function (VDF) of ions and sometimes electrons and SPAN is a combination of three electrostatic analyzers operated to measure the three dimensional VDFs of ions and electrons. Due to the instrument design, the SPAN-Ai instrument cannot observe the complete core of the solar wind ions in the first several encounters and SPC can provide ion observations during SPAN's observational gaps by pointing at the Sun during the encounter phase of each orbit, although SPC sometimes cannot detect the whole distribution (Kasper et al. 2016; Whittlesey et al. 2020; Case et al. 2020).

Therefore, we calculated the solar wind energy flux with both the RFS/FIELDS/PSP (electron) and SPC/SWEAP/PSP (ion) observations during Encounters One (E01), Two (E02), Four (E04), and Five (E05) (Section 2). The minimum heliocentric distance is 35.66 R_{\odot} for E01 and E02 and around 27.8 R_{\odot} for E04 and E05. In Section 3, we analyze the relationship between the energy flux, the bulk speed, and the plasma density (Section 3.1). How the total energy flux and each component of it evolve with increasing heliocentric distance is studied in Section 3.2. In Section 4, the results are summarized and discussed.

2. Data analysis

The solar wind energy flux (W), which includes the kinetic energy ($W_{kinetic}$), the enthalpy ($W_{enthalpy}$), and the heat flux (Q), is expressed as

$$W = W_{kinetic} + W_{enthalpy} + W_g + Q \quad (1)$$

where we have neglected the wave energy flux and added the flux equivalent to the energy required to overcome the solar gravitation W_g (Schwenn & Marsch 1990); Q is the sum of the electron heat flux q_e and proton heat flux q_p . Halekas et al. (2020a) and Halekas et al. (2020b) found that q_e ranges from 10^{-4} to 10^{-3} $W m^{-2}$ during E01, E02, E04, and E05 of PSP orbits, which can be neglected (See section 3). We note that at 1 AU, q_e measured with Helios is $q_e \approx 10^{-6}$ $W m^{-2}$ (Pilipp et al. 1990), while q_p ranges from about 10^{-7} (1 AU) to 10^{-5} (0.3 AU) $W m^{-2}$ (Hellinger et al. 2011). We therefore neglected both the

electron and proton heat flux compared to the other components, so that

$$W = W_{kinetic} + W_{enthalpy} + W_g \quad (2)$$

where the expressions of the different components are given below. It is important to note that Le Chat et al. (2012) neglected the enthalpy at 1 AU. However, this contribution cannot be ignored closer to the Sun, where it contributes to about 5% of the total energy flux (See section 3.2):

$$W_{kinetic} = n_p m_p V_p \frac{V_p^2}{2} + n_{\alpha} m_{\alpha} V_{\alpha} \frac{V_{\alpha}^2}{2} \quad (3)$$

$$\begin{aligned} W_{enthalpy} &= n_e V_p \frac{5k_B T_e}{2} + n_p V_p \frac{5k_B T_p}{2} + n_{\alpha} V_{\alpha} \frac{5k_B T_{\alpha}}{2} \\ &\approx n_e V_p \frac{5k_B T_e}{2} + n_p V_p \frac{5k_B T_p}{2} \end{aligned} \quad (4)$$

$$W_g = (n_p m_p V_p \frac{GM_{\odot}}{R_{\odot}} + n_{\alpha} m_{\alpha} V_{\alpha} \frac{GM_{\odot}}{R_{\odot}}) (1 - \frac{R_{\odot}}{r}) \quad (5)$$

Here, n_p , m_p , n_{α} , and m_{α} denote the proton number density, proton mass, α particle number density, and α particle mass, respectively. Furthermore, V_p (V_{α}) is the solar wind proton (α) bulk speed, n_e is the electron number density, k_B is the Boltzmann constant, T_p (T_e) is the proton (electron) temperature, G is the gravitational constant, M_{\odot} is the solar mass, R_{\odot} is the solar radius, and r is the heliocentric distance of PSP. We note that T_e was derived from the core electron temperature T_c and suprathermal electron temperature T_h with $T_e = T_c + (n_h/n_e)T_h$, where n_h denotes the suprathermal electron density and n_h/n_e is assumed to be 0.1 (see Moncuquet et al. 2020; Štverák et al. 2009). In Equation 3, 4, and 5, we assume that $V_{\alpha} \approx V_p$ and ignore the enthalpy of the α particles since n_{α} is much smaller than n_e (and both V_{α} and T_{α} are not available). The energy flux was scaled to one solar radius as written below, yielding the total energy required at the base to produce the wind – a basic quantity for understanding the wind production and comparing the Sun to other wind-producing stars:

$$W_{R_{\odot}} = W(r) \frac{r^2}{R_{\odot}^2}. \quad (6)$$

We used the level-3 ion data (moments) from SPC/SWEAP (Kasper et al. 2016; Case et al. 2020) and the electron parameters deduced from the simplified QTN method with the observations from RFS/FIELDS (Moncuquet et al. 2020; Pulupa et al. 2017). For each encounter, only 12-day high-time-resolution observations near the perihelion were considered: SPC collects one sample or more every 0.874 seconds and the QTN datasets have a 7-sec resolution. Since the resolution of the datasets from SPC is different from that of the QTN datasets, we interpolated them to the same resolution to carry out the calculations. Currently, α particle observations directly obtained from SPC/SWEAP cannot be used due to calibration issues. Also, n_p is too different from n_e (being smaller than n_e by more than 30% on average) with an estimation of $\langle n_{\alpha}/n_e \rangle = \langle (n_e - n_p) / (2 \times n_e) \rangle \approx 16.0\%$, which implies unrealistic values for n_{α} obtained based on plasma neutrality. Past studies (e.g., Kasper et al. 2007; Kasper et al. 2012; Alterman & Kasper 2019; Alterman et al. 2020) show

that the α particle abundance ($A_{He} = n_\alpha/n_p$) rarely exceeds $A_{He} \sim 5\%$, especially when the bulk speed of the solar wind is below $V_p = 400 \text{ km s}^{-1}$. [Alterman et al. \(2020\)](#) show that at 1 AU, A_{He} ranges from 1% to 5% during Solar Cycle 23 and 24 and predict that $1\% < A_{He} < 4\%$ at the onset of Solar Cycle 25 (solar minimum). We assume that A_{He} (which is almost the same as n_α/n_e) of the solar wind remains the same when it propagates from the inner heliosphere to 1 AU ([Viall & Borovsky 2020](#)). As a result, we deduced n_α with n_e where n_α/n_e is a free parameter ranging from 1% to 4% ([Alterman et al. 2020](#)). This enabled us to determine n_p based on the plasma neutrality. The resulting values of n_α and n_p were used to calculate W and then W_{R_\odot} .

3. Observations and results

During the first and second encounter of PSP, it reached the perihelion of $35.66 R_\odot$ ($\sim 0.17 \text{ AU}$) on November 6, 2018 and April 5, 2019, respectively. For both E04 and E05, PSP arrived at the perihelion of $27.8 R_\odot$ ($\sim 0.13 \text{ AU}$) on January 29, 2020 and June 7, 2020, respectively. In Section 3.1, we give an overview of the PSP measurements of solar wind density, speed, and energy flux for all available encounters including E01, E02, E04, and E05. We note that E03 observations are not considered due to the lack of SPC observations near the perihelion. For each encounter, 12-day observations around the perihelion were used for calculations. The heliocentric distance for both E01 and E02 ranges from 35.66 to about $55 R_\odot$, and it ranges from 27.8 to about $57 R_\odot$ for both E04 and E05. In Section 3.2, we combine the observations from E01, E02, E04, and E05 to show the histogram distributions and the evolution of the energy flux as a function of heliocentric distance.

3.1. Overview of E01, E02, E04, and E05

Figure 1 shows an overview of the PSP measurements of solar wind density, speed, and energy flux during E01 (from October 31, 2018 00:00:00 to November 12, 2018 00:00:00 UTC). The top panel presents the electron number density (n_e) obtained by the QTN method. In the second panel, the proton bulk speed is shown. The third and fourth panels present the solar wind energy flux (W , from equation 2) and its value scaled to one solar radius (W_{R_\odot} , from equation 6), respectively. In Figure 1, n_α and n_p were computed from n_e based on $n_\alpha/n_e = 2.5\%$ for calculating W and W_{R_\odot} . Most of the time, V_p varies around 300 km s^{-1} , and W_{R_\odot} varies around 70 W m^{-2} . The average values of W and W_{R_\odot} are 0.045 W m^{-2} and 77.3 W m^{-2} , respectively. The average value of W_{R_\odot} of E01 is consistent with the long-term observations from [Le Chat et al. \(2012\)](#) (around 79 W m^{-2}). We note that W_{R_\odot} does not vary much with V_p when V_p increases abruptly (i.e., from November 8 to 10, 2018).

Figure 2, which follows the same format as Figure 1, summarizes the PSP measurements of solar wind density, speed, and energy flux during E02 (from March 30, 2019 00:00:00 to April 11, 2019 00:00:00 UTC). We deduced n_p and n_α with the same method used for E01 to calculate both W and W_{R_\odot} . We note that n_e shows two successive low plateaus near the perihelion of E02 (from April 3 to 8, 2019 UT), as shown in the first panel of Figure 2, whereas V_p shows two high peaks. This is in agreement with the well-known anticorrelation between the solar wind speed and density (e.g., [Richardson et al. 1996](#); [Le Chat et al. 2012](#)). Both W_{R_\odot} and W also show two low plateaus near the perihelion of E02 (from April 3 to 8, 2019 UT), similar to the solar wind density. Elsewhere, V_p remains around 300 km s^{-1}

Table 1. Energy flux average value of each encounter.

Energy Flux (W m^{-2})	E01	E02	E04	E05
$\langle W \rangle$	0.045	0.032	0.054	0.057
$\langle W_{R_\odot} \rangle$	77.3	59.4	67.2	73.6

and W_{R_\odot} varies around 70 W m^{-2} . The mean values of W and W_{R_\odot} during E02 are 0.032 W m^{-2} and 59.4 W m^{-2} , respectively.

Similarly, Figure 3 illustrates the PSP observations during E04 (from January 23, 2020 00:00:00 to February 4, 2020 00:00:00 UTC). We used n_p and n_α , which were deduced with the same method used for both E01 and E02, when calculating both W and W_{R_\odot} . The second panel of Figure 3 shows that V_p varies around 375 km s^{-1} before January 29, 2020 and is predominantly 225 km s^{-1} afterward. Furthermore, W_{R_\odot} varies around 70 W m^{-2} and does not change significantly even when V_p decreases sharply from January 28 to 30, 2020. The average values of W and W_{R_\odot} for E04 are 0.054 W m^{-2} and 67.2 W m^{-2} , respectively.

Figure 4 is similar to Figure 1, 2, and 3, but for E05 (from June 1, 2020 00:00:00 to June 13, 2020 00:00:00 UTC). We used the same method as previously explained for E01, E02, and E04 for calculating the energy flux. During this encounter, V_p usually stays at around 300 km s^{-1} except from June 7 to 12, 2020 during which V_p remains approximately at 225 km s^{-1} . For E05, W_{R_\odot} is predominantly about $W_{R_\odot} = 70 \text{ W m}^{-2}$. From June 7 to 10, 2020, both W and W_{R_\odot} experience sharp changes, which results from a sharp variation in n_e . The corresponding values of both W and W_{R_\odot} are larger (smaller) than the ambient values at the beginning (in the end) of this time period. The average values of W and W_{R_\odot} for E05 are 0.057 W m^{-2} and 73.6 W m^{-2} , respectively.

Table 1 summarizes the average values of the energy flux $\langle W \rangle$ and the values normalized to one solar radius $\langle W_{R_\odot} \rangle$ for the four PSP encounters mentioned above. We note that the sequence difference between $\langle W_{R_\odot} \rangle$ and $\langle W \rangle$ results from the r^{-2} normalization when deriving W_{R_\odot} , whereas the individual flux tubes vary differently. It is remarkable that these values of $\langle W_{R_\odot} \rangle$ are close to those found previously ([Meyer-Vernet 2006](#); [Le Chat et al. 2012](#)) despite the smaller time durations and latitude extensions of PSP observations. We note the relatively low $\langle W_{R_\odot} \rangle$ of E02 and the low solar wind density near the perihelion of PSP orbit (see Figure 2). The dilute transient solar wind structure observed around the perihelion helps to explain this relatively low value compared to the long-term observations of [Le Chat et al. \(2012\)](#). The origins of the low plateaus of plasma density related to high peaks of bulk speed are discussed by [Rouillard et al. \(2020\)](#) and they are outside the scope of this paper. [Le Chat et al. \(2012\)](#) averaged the values over a solar rotation (~ 27.2 days) to reduce the effect of transient events such as coronal mass ejections (CMEs) or corotating interaction regions (CIRs). Although CMEs or small-scale flux ropes are observed by PSP during E01 (e.g., [Hess et al. 2020](#); [Zhao et al. 2020](#); [Korreck et al. 2020](#)), $\langle W_{R_\odot} \rangle$ of E01 (77.3 W m^{-2}) is almost the same as the long-term averaged value found by [Le Chat et al. \(2012\)](#).

3.2. Distributions of energy flux and variation with distance

Figure 5 shows the distributions of W_{R_\odot} combining the observations from E01, E02, E04, and E05. Based on the assumption that n_α/n_e ranges from 1.0% to 4.0%, we calculated W_{R_\odot} with $n_\alpha/n_e = 1.0\%$, 2.5% , and 4.0% and the corresponding results are shown in Figure 5 (a), (b), and (c), respectively. Each histogram

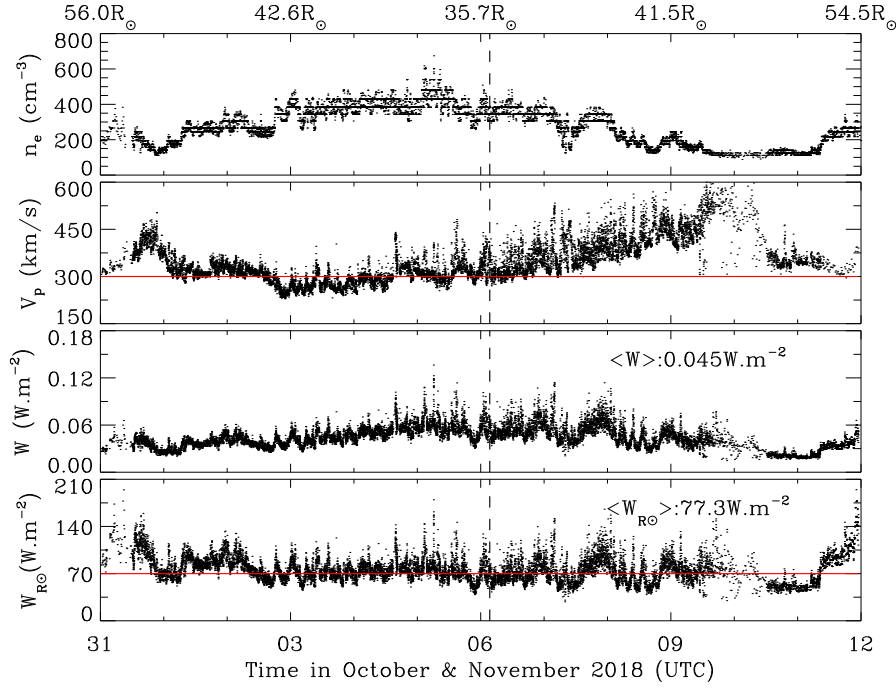


Fig. 1. Solar wind density, speed, and energy flux measurements by PSP during Encounter One (from October 31, 2018 00:00:00 to November 12, 2018 00:00:00 UTC). First panel: QTN electron density. Second panel: Proton bulk speed. A red horizontal line ($V_p = 300 \text{ km s}^{-1}$) is plotted for reference. Third panel: Solar wind energy flux W . Fourth panel: Solar wind energy flux normalized to one solar radius W_{R_\odot} (black) with a red horizontal line ($W_{R_\odot} = 70 \text{ W m}^{-2}$) superimposed for reference. The heliocentric distance (in units of the Solar radius R_\odot) is indicated at the top of the first panel and the black vertical line denotes the perihelion of the PSP orbit.

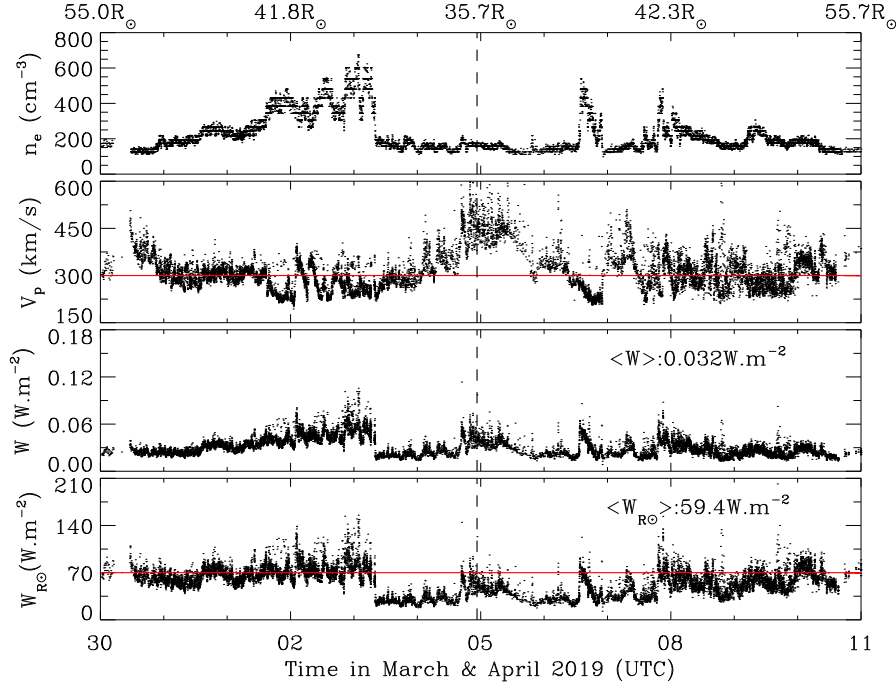


Fig. 2. Solar wind density, speed, and energy flux measurements by PSP for Encounter Two (March 30, 2019 00:00:00 to April 11, 2019 00:00:00 UTC). This figure follows the same format as that of Figure 1.

distribution was fitted with a Gaussian function (blue line), and the center value (the most probable value) and standard deviation (full-width-half-maximum which is short for FWHM) are shown together with the mean and median values. It is remarkable that the histograms of W_{R_\odot} are very symmetrical and nearly

Gaussian. The difference between the average, median, and most probable fit value of W_{R_\odot} is very small (less than 3%). With a fixed n_α/n_e ratio, the uncertainties of $\langle W_{R_\odot} \rangle$ resulting from the uncertainties of the plasma parameters n_e , V_p , T_e , and T_p are 10.0%, 4.1%, 0.85%, and 0.28%, respectively. We used the un-

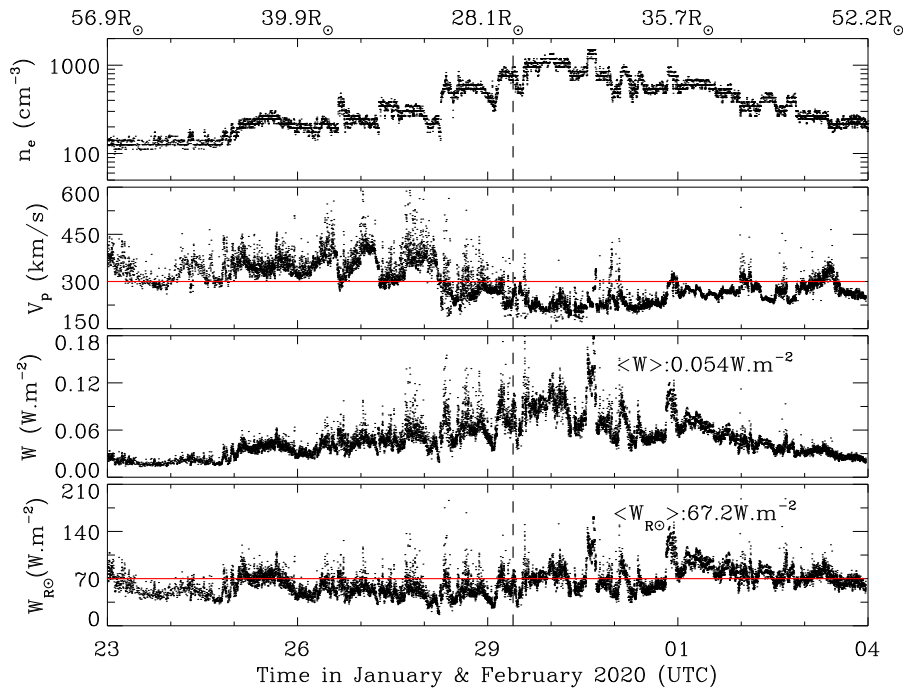


Fig. 3. Solar wind density, speed, and energy flux measurements by PSP for Encounter Four (from January 23, 2020 00:00:00 to February 4, 2020 00:00:00 UTC), which follows the same format as that of Figure 1.

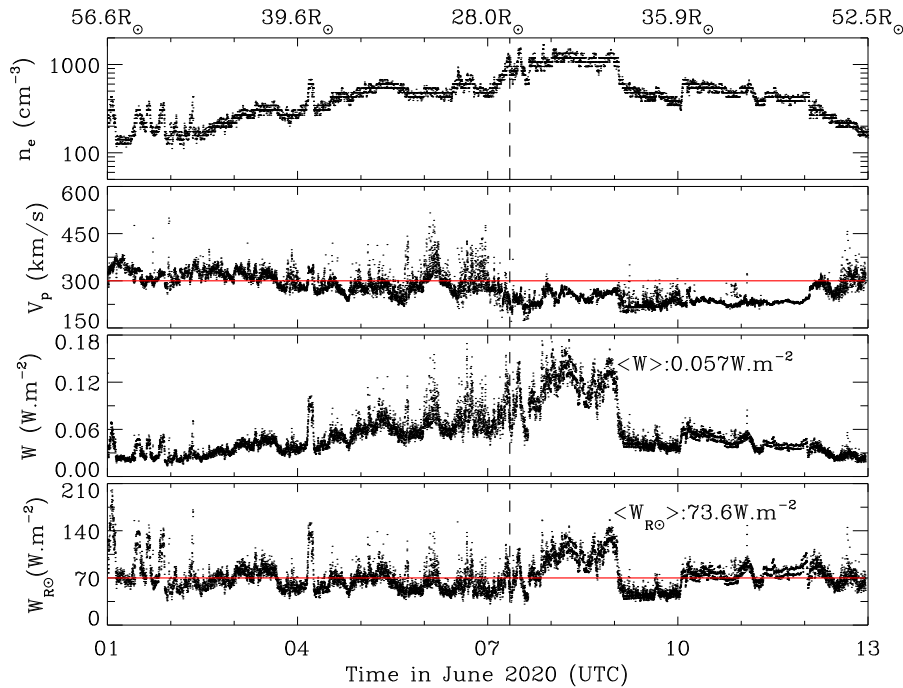


Fig. 4. Solar wind density, speed, and energy flux measurements by PSP for Encounter Five (from June 1, 2020 00:00:00 to June 13, 2020 00:00:00 UTC), which follows the same format as that of Figure 1.

certainty of n_e provided by the QTN method and [Moncuquet et al. \(2020\)](#) estimate that the uncertainty of T_e is around 20%. [Case et al. \(2020\)](#) share that the estimated uncertainties of V_p and T_p are 3.0% and 19%, respectively. When n_α/n_e increases from 1.0% to 2.5% and then to 4.0%, $\langle W_{R_\odot} \rangle$ increases from 66.7 W m⁻² to 69.4 W m⁻² and then to 72.1 W m⁻², and the values of FWHM increase from 41.2 W m⁻² to 42.7 W m⁻² and then to 44.4 W m⁻². The uncertainty of W_{R_\odot} resulting from the varia-

tion of n_α/n_e is around 4%. Furthermore, $\langle W_{R_\odot} \rangle$ from the E01, E02, E04, and E05 observations is around 69.4 W m⁻² with a total uncertainty that we estimate to be at most 20.0%, which is consistent with previous results (e.g., [Schwenn & Marsch 1990](#); [Meyer-Vernet 2006](#); [Le Chat et al. 2009, 2012](#); [McComas et al. 2014](#)).

Figure 6 presents W , $W_{kinetic}/W$, $W_{enthalpy}/W$, and W_g/W as a function of heliocentric distance in units of solar radius R_\odot ,

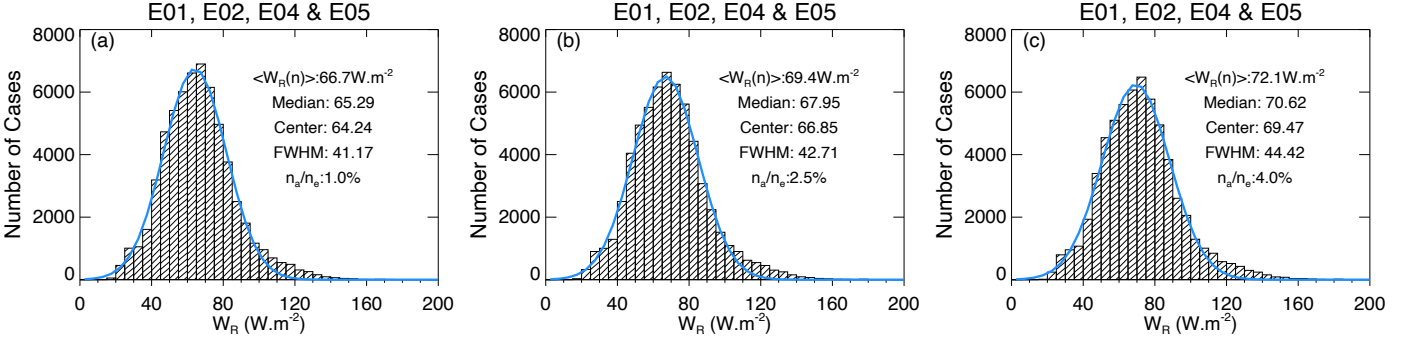


Fig. 5. Distributions of solar wind energy flux (W_R) normalized to one solar radius with a ratio between α particle number density (n_α) and electron number density (n_e) ranging from 1% to 4% for Encounters E01, E02, E04, and E05. Figs (a), (b), and (c) assume $n_\alpha/n_e = 1\%$, 2.5% , and 4% , respectively, to illustrate the uncertainty due to the absence of α measurements. Average and median values of each histogram are indicated with Gaussian fits superimposed in blue. Center value and standard deviation (full-width-half-maximum) of the Gaussian fit are also presented.

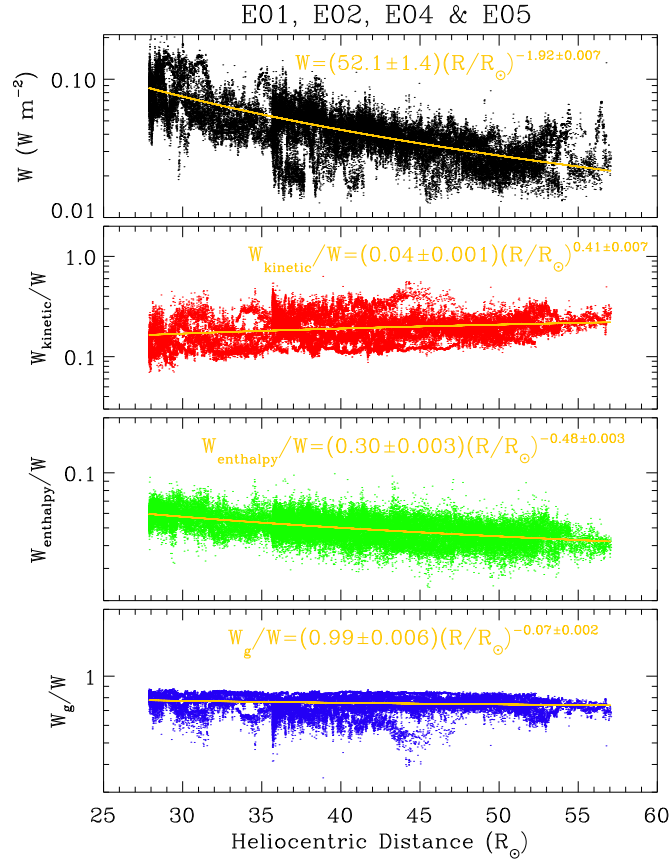


Fig. 6. Variation of W and its components with heliocentric distance combining observations from Encounter One (E01), Two (E02), Four (E04), and Five (E05). From top to bottom, evolution of W , $W_{kinetic}/W$, $W_{enthalpy}/W$, and W_g/W with heliocentric distance are shown, respectively. The fitted profile (yellow) is superimposed on each corresponding panel, respectively.

which includes the observations from E01, E02, E04, and E05. Levenberg-Marquardt least-squares fit was performed on each quantity and the fitted functions are shown in the figure. We note that the power index for W is -1.92 (near to -2.0), which is in agreement with Equation 6 used to scale the solar wind energy flux to one R_\odot . When PSP moves from $57.1 R_\odot$ to $27.8 R_\odot$, $W_{kinetic}$, in order of magnitude, ranges from 10^{-3} to $10^{-2} W m^{-2}$, while $W_{enthalpy}$ and W_g range from 10^{-3} to $10^{-2} W m^{-2}$ and from 10^{-2} to $10^{-1} W m^{-2}$, respectively. Further, as shown in Figure 6, W_g is the dominant term for W , $W_{kinetic}$ is the second most dominant one, and $W_{enthalpy}$ is the least dominant term. Even though

the contribution of $W_{enthalpy}$ to W is still the least among the three components in the inner heliosphere, it reaches about 30% of the kinetic energy flux at the smallest distances and we cannot neglect it directly ($\langle W_{enthalpy} \rangle / \langle W \rangle \approx 5\%$). We note that since W_g exceeds $W_{kinetic}$ by a factor of about four, most of the energy supplied by the Sun to generate the solar wind serves to overcome the solar gravity. As is shown in the first panel of Figure 6, the energy flux can reach $W \approx 10^{-1} W m^{-2}$ near the perihelia of PSP orbits, whereas the corresponding electron heat flux is $q_e \approx 10^{-3} W m^{-2}$ (see Halekas et al. 2020a,b). At most, q_e contributes to 1.0% of W , and proton heat flux q_p is usually much less than q_e .

Therefore, neglecting the heat flux does not affect the conclusions made in this work.

4. Discussion and conclusions

This paper presents the first analysis of the solar wind energy flux in the inner heliosphere (adding the flux equivalent to the energy necessary to move the wind out of the solar gravitational potential) with PSP observations. This covers heliocentric distances from 0.13 AU ($\sim 27.8 R_{\odot}$) to 0.27 AU ($\sim 57.1 R_{\odot}$) in combination of data during E01, E02, E04, and E05. This enables us to study the solar wind energy flux in the inner heliosphere, which is of great importance to understand the acceleration of the solar wind. We note that E03 is excluded due to the lack of SPC observations near perihelion.

We find that the average value of $W_{R_{\odot}}$, $\langle W_{R_{\odot}} \rangle$, is about 69.4 W m^{-2} with a total uncertainty of at most 20%, which is similar to previous results based on long-term observations at greater distances and various latitudes (e.g., Schwenn & Marsch 1990; Meyer-Vernet 2006; Le Chat et al. 2009, 2012; McComas et al. 2014). This result confirms that this quantity appears as a global solar constant, which is of importance since it is often used to deduce the solar wind density from the speed (or the reverse) in global heliospheric studies and modeling (e.g., Shen et al. 2018; McComas et al. 2014, 2017, 2020; Krimigis et al. 2019; Wang et al. 2020).

It is remarkable that the distributions of $W_{R_{\odot}}$ are nearly symmetrical and well fitted by Gaussians. This may be explained by the limited interactions between solar wind and transient structures (e.g., CMEs and CIRs) in the inner heliosphere (below 0.27 AU).

Normalizing the solar wind energy flux as $1/r^2$ assumes a radial expansion of solar wind, which does not hold true for individual flux tubes, especially close to the Sun. However, this normalization holds true when integrating over a whole sphere surrounding the Sun, so that a large data set is necessary to obtain a reliable result. It is thus noteworthy that with only 12-day observations for each encounter (E01, E02, E04, and E05) and a limited latitude exploration, we find the same normalized energy flux as previous long-term studies at various latitudes. This is consistent with the fact that our dataset yields an energy flux varying with heliocentric distance with a power index close to -2. It is also interesting that this normalized energy flux represents a similar fraction of solar luminosity as observed for a large quantity of stars (Meyer-Vernet 2006; Le Chat et al. 2012). Since this quantity represents the energy flux to be supplied by the Sun for producing the wind (e.g., Meyer-Vernet 1999; Schwadron & McComas 2003), this similarity may provide clues to the physical processes at the origin of stellar winds (e.g., Johnstone et al. 2015).

In this work, the heat flux was neglected when calculating the energy flux. When PSP gets much closer to the Sun, the contribution of the electron heat flux is larger (see Halekas et al. 2020a,b). Furthermore, the solar wind protons often consist of two populations, that is to say core and beam drifting with respect to each other. The speed difference between them is typically on the order of the local Alfvén speed (Alterman et al. 2018). It is likely that the proton heat flux will also be more important closer to the Sun. Therefore, the heat flux will be considered in a future work. Due to the lack of alpha particle observations, we make an assumption that $V_{\alpha} \approx V_p$. In fact, the differential speed between protons and alpha particles is also typically on the order of the local Alfvén speed (e.g., Steinberg et al. 1996;

Đurovcová et al. 2017; Alterman et al. 2018), so that it may affect the energy flux closer to the Sun. We await more data that are to come in the future PSP encounters, with the recovery of the well calibrated alpha parameters.

Acknowledgements. The research was supported by the CNES and DIM ACAV+ PhD funding. Parker Solar Probe was designed, built, and is now operated by the Johns Hopkins Applied Physics Laboratory as part of NASA's Living with a Star (LWS) program (contract NNN06AA01C). Support from the LWS management and technical team has played a critical role in the success of the Parker Solar Probe mission. We acknowledge the use of data from FIELDS/PSP (<http://research.ssl.berkeley.edu/data/psp/data/sci/fields/l2/>) and SWEAP/PSP (<http://sweap.cfa.harvard.edu/pub/data/sci/sweap/>).

References

- Alterman, B. L. & Kasper, J. C. 2019, *ApJ*, 879, L6
 Alterman, B. L., Kasper, J. C., Leamon, R. J., & McIntosh, S. W. 2020, arXiv e-prints, arXiv:2006.04669
 Alterman, B. L., Kasper, J. C., Stevens, M. L., & Koval, A. 2018, *ApJ*, 864, 112
 Bale, S. D., Goetz, K., Harvey, P. R., et al. 2016, *Space Sci. Rev.*, 204, 49
 Case, A. W., Kasper, J. C., Stevens, M. L., et al. 2020, *ApJS*, 246, 43
 Fox, N. J., Velli, M. C., Bale, S. D., et al. 2016, *Space Sci. Rev.*, 204, 7
 Halekas, J. S., Whittlesey, P., Larson, D. E., et al. 2020a, *A&A*, accepted, same series
 Halekas, J. S., Whittlesey, P., Larson, D. E., et al. 2020b, *ApJS*, 246, 22
 Hellinger, P., Matteini, L., Štverák, Š., Trávníček, P. M., & Marsch, E. 2011, *Journal of Geophysical Research (Space Physics)*, 116, A09105
 Hess, P., Rouillard, A. P., Kouloumvakos, A., et al. 2020, *ApJS*, 246, 25
 Issautier, K., Hoang, S., Moncuquet, M., & Meyer-Vernet, N. 2001, *Space Sci. Rev.*, 97, 105
 Issautier, K., Le Chat, G., Meyer-Vernet, N., et al. 2008, *Geophys. Res. Lett.*, 35, L19101
 Issautier, K., Meyer-Vernet, N., Moncuquet, M., Hoang, S., & McComas, D. J. 1999, *J. Geophys. Res.*, 104, 6691
 Johnstone, C. P., Güdel, M., Lüftinger, T., Toth, G., & Brott, I. 2015, *A&A*, 577, A27
 Kasper, J. C., Abiad, R., Austin, G., et al. 2016, *Space Sci. Rev.*, 204, 131
 Kasper, J. C., Stevens, M. L., Korreck, K. E., et al. 2012, *ApJ*, 745, 162
 Kasper, J. C., Stevens, M. L., Lazarus, A. J., Steinberg, J. T., & Ogilvie, K. W. 2007, *ApJ*, 660, 901
 Korreck, K. E., Szabo, A., Nieves Chinchilla, T., et al. 2020, *ApJS*, 246, 69
 Krimigis, S. M., Decker, R. B., Roelof, E. C., et al. 2019, *Nature Astronomy*, 3, 997
 Le Chat, G., Issautier, K., & Meyer-Vernet, N. 2012, *Sol. Phys.*, 279, 197
 Le Chat, G., Meyer-Vernet, N., & Issautier, K. 2009, in *American Institute of Physics Conference Series*, Vol. 1094, 15th Cambridge Workshop on Cool Stars, Stellar Systems, and the Sun, ed. E. Stempels, 365–368
 Maksimovic, M., Bale, S. D., Berčič, L., et al. 2020, *ApJS*, 246, 62
 Maksimovic, M., Hoang, S., Meyer-Vernet, N., et al. 1995, *J. Geophys. Res.*, 100, 19881
 McComas, D. J., Alexander, N., Angold, N., et al. 2016, *Space Sci. Rev.*, 204, 187
 McComas, D. J., Allegrini, F., Bzowski, M., et al. 2014, *ApJS*, 213, 20
 McComas, D. J., Bzowski, M., Dayeh, M. A., et al. 2020, *ApJS*, 248, 26
 McComas, D. J., Zirnstein, E. J., Bzowski, M., et al. 2017, *ApJS*, 229, 41
 Meyer-Vernet, N. 1979, *J. Geophys. Res.*, 84, 5373
 Meyer-Vernet, N. 1999, *European Journal of Physics*, 20, 167
 Meyer-Vernet, N. 2006, in *IAU Symposium*, Vol. 233, *Solar Activity and its Magnetic Origin*, ed. V. Bothmer & A. A. Hady, 269–276
 Meyer-Vernet, N. 2007, *Basics of the Solar Wind*
 Meyer-Vernet, N., Couturier, P., Hoang, S., et al. 1986, *Science*, 232, 370
 Meyer-Vernet, N., Issautier, K., & Moncuquet, M. 2017, *J. Geophys. Res.*, 122, 7925
 Moncuquet, M., Lecacheux, A., Meyer-Vernet, N., Cecconi, B., & Kurth, W. S. 2005, *Geophys. Res. Lett.*, 32, L20S02
 Moncuquet, M., Matsumoto, H., Bougeret, J. L., et al. 2006, *Advances in Space Research*, 38, 680
 Moncuquet, M., Meyer-Vernet, N., Issautier, K., et al. 2020, *ApJS*, 246, 44
 Neugebauer, M. & Snyder, C. W. 1962, *Science*, 138, 1095
 Parker, E. N. 1958, *ApJ*, 128, 664
 Parker, E. N. 2001, *Ap&SS*, 277, 1
 Pilipp, W. G., Muehlhaeuser, K. H., Miggenrieder, H., Rosenbauer, H., & Schwenn, R. 1990, *J. Geophys. Res.*, 95, 6305
 Pulupa, M., Bale, S. D., Bonnell, J. W., et al. 2017, *J. Geophys. Res.*, 122, 2836
 Richardson, J. D., Belcher, J. W., Lazarus, A. J., Paularena, K. I., & Gazis, P. R. 1996, *AIP Conference Proceedings*, 382, 483

- Rouillard, A. P., Kouloumvakos, A., Vourlidas, A., et al. 2020, ApJS, 246, 37
- Schwadron, N. A. & McComas, D. J. 2003, ApJ, 599, 1395
- Schwenn, R. & Marsch, E. 1990, Physics and Chemistry in Space, 20
- Schwenn, R., Rosenbauer, H., & Miggenrieder, H. 1975, Raumfahrtforschung, 19, 226
- Shen, F., Yang, Z., Zhang, J., Wei, W., & Feng, X. 2018, ApJ, 866, 18
- Steinberg, J. T., Lazarus, A. J., Ogilvie, K. W., Lepping, R., & Byrnes, J. 1996, Geophys. Res. Lett., 23, 1183
- Štverák, T., Šafránková, J., Němeček, Z., & Richardson, J. D. 2017, ApJ, 850, 164
- Viall, N. M. & Borovsky, J. E. 2020, Journal of Geophysical Research (Space Physics), 125, e26005
- Vourlidas, A., Howard, R. A., Plunkett, S. P., et al. 2016, Space Sci. Rev., 204, 83
- Štverák, Š., Maksimovic, M., Trávníček, P. M., et al. 2009, J. Geophys. Res., 114, A05104
- Wang, Y. X., Guo, X. C., Wang, C., et al. 2020, Space Weather, 18, e02262
- Wenzel, K. P., Marsden, R. G., Page, D. E., & Smith, E. J. 1992, A&AS, 92, 207
- Whittlesey, P. L., Larson, D. E., Kasper, J. C., et al. 2020, ApJS, 246, 74
- Zhao, L. L., Zank, G. P., Adhikari, L., et al. 2020, ApJS, 246, 26